Electromagnetic tomography of spin- $\frac{3}{2}$ hidden-charm strange pentaquarks

Ulaş Özdem⁰^{1,∗}

¹Health Services Vocational School of Higher Education, Istanbul Aydin University, Sefakoy-Kucukcekmece, 34295 Istanbul, Türkiye

Understanding how quarks are spatially arranged inside exotic pentaquarks remains one of the key open problems in contemporary hadron spectroscopy. The electromagnetic multipole moments of hadrons provide a direct probe of their internal quark–gluon geometry and spatial charge distributions. Motivated by this, we employ QCD light-cone sum rules to compute the magnetic dipole, electric quadrupole, and magnetic octupole moments of the $J^P = 3/2^-$ pentaquark with strangeness S = -1. Five distinct diquark–diquark–antiquark interpolating currents are constructed to explore possible internal configurations. The resulting electromagnetic moments exhibit pronounced sensitivity to the underlying quark arrangement: magnetic dipole moments range from $-2.28\mu_N$ to $+3.36\mu_N$, establishing this observable as a key discriminator among configurations with identical quantum numbers. Nonzero electric quadrupole and magnetic octupole moments indicate clear deviations from spherical symmetry, while a detailed decomposition shows that light quarks dominate the magnetic response and the charm quark drives quadrupole deformation. These findings position electromagnetic multipole moments as quantitative and discriminating probes of exotic hadron structure, providing concrete benchmarks for forthcoming LHCb, Belle II, and lattice QCD studies.

I. MOTIVATION

The concept of hadronic states beyond the conventional quark-antiquark mesons and three-quark baryons has been proposed for many decades. Experimental verification of such exotic configurations was first achieved in 2003 with the discovery of the X(3872) by the Belle Collaboration [1]. Due to its properties that cannot be explained within the framework of standard mesons, this state is widely regarded as the first confirmed tetraquark candidate. Since then, numerous exotic hadrons featuring nontraditional quark arrangements have been observed, and the variety of these states has steadily expanded. These findings have stimulated extensive theoretical and experimental studies aimed at understanding the nature and internal structure of these unconventional multi-quark systems, which in turn provide valuable information on the dynamics of strong interactions at low energies. A range of theoretical interpretations has been proposed, including compact multiquark models, hadronic molecules, and explanations based on kinematic effects, among others [2–17]. Together, these efforts have significantly advanced our understanding of exotic hadronic matter and continue to guide ongoing research in hadron spectroscopy.

In 2015, the LHCb Collaboration achieved a significant milestone in the study of exotic multi-quark hadrons by reporting two pentaquark states, denoted $P_{\psi}^{N}(4380)$ and $P_{\psi}^{N}(4450)$, observed in the $J/\psi p$ invariant mass spectrum from the decay $\Lambda_b^0 \to J/\psi p K^-$. Later, with an updated analysis incorporating data from both Run I and Run II, the LHCb Collaboration refined their observations of the $J/\psi p$ spectrum in $\Lambda_b \to J/\psi p K$ decays. This analysis revealed a new pentaquark, $P_\psi^N(4312)$, and resolved the previously reported $P_\psi^N(4450)$ into two distinct states, labeled $P_\psi^N(4440)$ and $P_\psi^N(4457)$. The status of $P_\psi^N(4380)$, however, remains inconclusive in the updated study, leaving its existence uncertain. Since these states appear in the $J/\psi p$ channel, their minimal quark content is expected to be $uudc\bar{c}$. Building on these discoveries, the LHCb Collaboration extended the search for hidden-charm pentaquarks with strangeness. In 2020, they reported evidence for a candidate state, $P_{\psi s}^{\Lambda}(4459)$, in the $J/\psi\Lambda$ invariant mass spectrum from the decay $\Xi_b^- \to J/\psi \Lambda K^-$. Subsequently, in 2022, another candidate, $P_{\psi s}^{\Lambda}(4338)$, was observed in the same channel. The quark composition of these $P_{\psi s}^{\Lambda}$ states is generally assumed to be $udsc\bar{c}$, consistent with their decay products. The masses and decay widths of these pentaquark states can be seen in Refs. [18-21]. Very recently, the Belle Collaboration reported evidence for a $P_{\psi s}^{\Lambda}$ state, achieving a significance of 3.3σ when both statistical and systematic uncertainties are taken into account. The measured mass and width of this state are (4471.7±4.8±0.6) MeV and $(21.9 \pm 13.1 \pm 2.7)$ MeV, respectively [22]. Nevertheless, given the limited available data, one cannot exclude the possibility that the observed signal originates from two separate states. The study further indicates that the observed state could correspond to a different state in the same mass region [23]. This possibility points to overlapping or closely spaced resonances, emphasizing the need for careful experimental and theoretical analysis to accurately determine the nature and quantum numbers of the observed state.

^{*} ulasozdem@aydin.edu.tr

The spin and parity of the hidden-charm pentaquark states have not yet been experimentally established. Despite significant theoretical and experimental efforts following their initial discovery, the underlying nature and internal structure of these exotic states remain largely unresolved. This lack of definitive information underscores the importance of further detailed studies aimed at uncovering their properties. A thorough understanding of these systems requires the investigation of various observables that probe the internal dynamics of the states. Quantities such as decay constants, branching ratios, and transition form factors provide critical insights into their quark-gluon composition and interaction patterns. Among these, electromagnetic properties, and in particular magnetic moments, constitute especially valuable probes. Magnetic moments not only quantify the distribution of charge and magnetization within the hadron but also offer a direct window into the spatial arrangement and spin alignment of constituent quarks. By analyzing these moments, one can infer key aspects of the internal configuration, such as the role of different quark flavors and possible deformation patterns, thereby complementing other experimental and theoretical investigations and guiding future studies aimed at resolving the true nature of hidden-charm pentaquarks.

Inspired by these developments, the growing interest in hidden-charm pentaquark states, and the open questions that still need to be addressed, in this work, we present a systematic analysis of the magnetic dipole, electric quadrupole, and magnetic octupole moments of hidden-charm pentaquarks with strangeness S=-1, employing the framework of QCD light-cone sum rules [24–26]. Our study considers five distinct interpolating currents constructed in diquark-diquark-antiquark configurations, chosen for their expected effectiveness in coupling to pentaquark states with $J^P=3/2^-$. Electromagnetic interactions provide a fundamental and non-invasive probe of the spatial and dynamical properties of quarks and gluons inside hadrons. These interactions are described through elastic and inelastic multipole form factors, which encode detailed information on the internal geometry of hadrons, including their shape, size, and charge and current distributions (See Fig. 1). The multipole moments, as leading-order responses to external electromagnetic fields, offer particularly direct insight into the structural characteristics of hadronic states. The topic has attracted growing attention in the literature due to the valuable insights it provides, with numerous studies employing a range of models and techniques to investigate the electromagnetic multipole moments of hidden-charm and hidden-bottom pentaquarks [27–53].

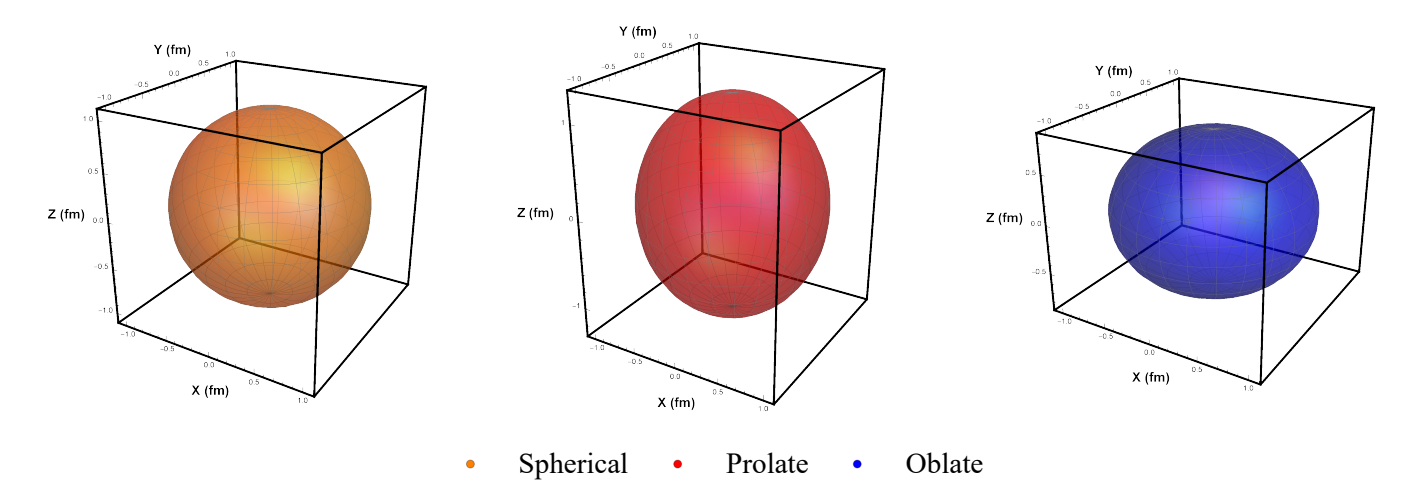


FIG. 1. Illustrates the charge distributions corresponding to intrinsic quadrupole moments (Q): spherical (Q = 0), positive (prolate, Q > 0), and negative (oblate, Q < 0). Similarly, a structural asymmetry is observed for the octupole moment (Q).

The paper is structured as follows. In the next section, we describe the methodology used to construct suitable interpolating currents for the $P_{\psi s}^{\Lambda}$ pentaquark and derive the corresponding sum rules for the physical observables of interest. The numerical analysis and associated discussions are presented in Sec. III. A detailed structural interpretation of the results and the corresponding experimental signatures are presented in Sec. IV. Finally, we conclude with a summary of the main findings and implications of this work in Sec. V.

II. QCD LIGHT-CONE SUM RULES SETUP

The first step in the calculation involves the definition of an appropriate correlation function that encapsulates the relevant quantum numbers and interpolating currents of the system under study. For the analysis of the electromag-

netic multipole moments of the $P_{\psi s}^{\Lambda}$ state, the correlation function is constructed as follows:

$$T_{\mu\nu}(p,q) = i \int d^4x e^{ip \cdot x} \langle 0|T \{J_{\mu}(x)\bar{J}_{\nu}(0)\} |0\rangle_F.$$
 (1)

Here, F represents the external electromagnetic field that induces the interaction responsible for the multipole transitions, while $J_{\mu}(x)$ denotes the interpolating current corresponding to the $P_{\psi s}^{\Lambda}$ state. The possible interpolating currents that couple to the $P_{\psi s}^{\Lambda}$ state are given as:

$$J_{\mu}^{1}(x) = \frac{\mathcal{A}}{\sqrt{2}} \left\{ \left[u_{d}^{T}(x) C \gamma_{5} s_{e}(x) \right] \left[d_{f}^{T}(x) C \gamma_{\mu} c_{g}(x) \right] - \left[d_{d}^{T}(x) C \gamma_{5} s_{e}(x) \right] \left[u_{f}^{T}(x) C \gamma_{\mu} c_{g}(x) \right] \right\} C \bar{c}_{c}^{T}(x), \qquad (2)$$

$$J_{\mu}^{2}(x) = \frac{\mathcal{A}}{\sqrt{2}} \left\{ \left[u_{d}^{T}(x) C \gamma_{\mu} s_{e}(x) \right] \left[d_{f}^{T}(x) C \gamma_{5} c_{g}(x) \right] - \left[d_{d}^{T}(x) C \gamma_{\mu} s_{e}(x) \right] \left[u_{f}^{T}(x) C \gamma_{5} c_{g}(x) \right] \right\} C \bar{c}_{c}^{T}(x), \tag{3}$$

$$J_{\mu}^{3}(x) = \frac{\mathcal{A}}{\sqrt{2}} \left\{ \left[u_{d}^{T}(x) C \gamma_{\mu} s_{e}(x) \right] \left[d_{f}^{T}(x) C \gamma_{\alpha} c_{g}(x) \right] - \left[d_{d}^{T}(x) C \gamma_{\mu} s_{e}(x) \right] \left[u_{f}^{T}(x) C \gamma_{\alpha} c_{g}(x) \right] \right\} \gamma_{5} \gamma^{\alpha} C \bar{c}_{c}^{T}(x), \qquad (4)$$

$$J_{\mu}^{4}(x) = \frac{\mathcal{A}}{\sqrt{2}} \left\{ \left[u_{d}^{T}(x) C \gamma_{\alpha} s_{e}(x) \right] \left[d_{f}^{T}(x) C \gamma_{\mu} c_{g}(x) \right] - \left[d_{d}^{T}(x) C \gamma_{\alpha} s_{e}(x) \right] \left[u_{f}^{T}(x) C \gamma_{\mu} c_{g}(x) \right] \right\} \gamma_{5} \gamma^{\alpha} C \bar{c}_{c}^{T}(x), \qquad (5)$$

$$J^{5}_{\mu}(x) = \mathcal{A}\left\{\left[u^{T}_{d}(x)C\gamma_{5}d_{e}(x)\right]\left[s^{T}_{f}(x)C\gamma_{\mu}c_{g}(x)\right]\right\}C\bar{c}^{T}_{c}(x), \qquad (6)$$

where $\mathcal{A} = \varepsilon_{abc}\varepsilon_{ade}\varepsilon_{bfg}$, with a, b, c, d, e, f, and g denoting color indices, and C representing the charge conjugation operator.

The five interpolating currents $J^1_{\mu}(x)$ – $J^5_{\mu}(x)$ are constructed to probe distinct configurations within the complex wavefunction of a $J^P = \frac{3}{2}$ hidden-charm strange pentaquark. All currents are carefully built to maintain the correct quantum numbers while emphasizing different diquark correlations and spatial arrangements, thereby allowing us to assess the structural sensitivity of electromagnetic observables across a broad spectrum of possible internal organizations. A more detailed justification for this quintuple current approach is as follows: $J^1_{\mu}(x)$, the scalar-axial-vector current, combines a scalar light-strange diquark $[u^T C \gamma_5 s]$ with an axial-vector charm-light diquark $[d^T C \gamma_\mu c]$. While this configuration primarily emphasizes compact diquark correlations, its specific structure may also allow coupling to molecular-type configurations where distinct meson-baryon components could overlap with this diquark arrangement. The current $J^2_{\mu}(x)$, the axial-vector-scalar current, reverses the diquark roles compared to J^1_{μ} , employing an axial-vector light-strange diquark $[u^T C \gamma_{\mu} s]$ with a scalar charm-light diquark $[d^T C \gamma_5 c]$. This swapped arrangement probes how the assignment of scalar versus axial-vector character to heavy and light diquarks affects the electromagnetic properties, while maintaining the possibility of overlap with both compact and molecular configurations through different diquark clustering patterns. Meanwhile, $J^3_{\mu}(x)$ and $J^4_{\mu}(x)$ both represent axial-vector-axial-vector configurations but with crucial differences in Lorentz index assignments. J_{μ}^3 places the Lorentz index α in the charm-containing diquark $[d^T C \gamma_{\alpha} c]$, while J^4_{μ} positions it in the light-strange diquark $[u^T C \gamma_{\alpha} s]$. Both employ the $\gamma_5 \gamma^{\alpha}$ structure for correct angular momentum coupling. These currents are primarily optimized for probing compact multiquark states with strong color correlations, as their symmetric axial-vector diquark structures favor tightly bound configurations. While the possibility of coupling to specific molecular arrangements cannot be entirely excluded—particularly those with correlated spin structures that might overlap with these diquark combinations—their design makes them most sensitive to genuine compact pentaquark components. Finally, $J^5_{\mu}(x)$, the unique non-strange-strange separated current, features a scalar non-strange diquark $[u^T C \gamma_5 d]$ coupled to an axial-vector strange-charm diquark $[s^T C \gamma_\mu c]$. This clear separation between non-strange and strange-heavy sectors suggests strong overlap with compact configurations featuring distinct quark sector clustering, while the specific diquark combinations may also permit coupling to certain molecular-type wavefunctions. By employing this set of five currents, we effectively scan a comprehensive range of possible internal structures within the hidden-charm strange pentaquark spectrum. The significant variation in predicted multipole moments across these currents provides a quantitative measure of how sensitively these fundamental observables depend on the underlying quark-gluon architecture, revealing the rich structural diversity accessible even within the same quantum number sector, without presupposing the dominance of any particular structural model. It should be noted that QCD sum rules suggest the scalar and axial-vector diquark configurations to be the most favorable for studying hadronic properties [54, 55]. Accordingly, the interpolating currents introduced above are constructed in various combinations based on these configurations.

In the hadronic framework, the principle of quark-hadron duality is employed to transform the correlation function into its hadronic representation. This is achieved by inserting a complete set of intermediate states possessing the

same quantum numbers as the interpolating currents. The contribution from the ground state, denoted as $P_{\psi s}^{\Lambda}$, is isolated from those of higher-energy states and the continuum, yielding the following expression:

$$T_{\mu\nu}^{Had}(p,q) = \frac{\langle 0 \mid J_{\mu}(x) \mid P_{\psi s}^{\Lambda}(p_{2},s) \rangle}{[p_{2}^{2} - m_{P_{\psi s}^{\Lambda}}^{2}]} \langle P_{\psi s}^{\Lambda}(p_{2},s) \mid P_{\psi s}^{\Lambda}(p_{1},s) \rangle_{F} \frac{\langle P_{\psi s}^{\Lambda}(p_{1},s) \mid \bar{J}_{\nu}(0) \mid 0 \rangle}{[p_{1}^{2} - m_{P_{\psi s}^{\Lambda}}^{2}]} + \text{higher states and continuum.}$$
(7)

Here, $p_1 = p + q$, $p_2 = p$, and q denotes the momentum of the photon. The evaluation of this correlation function requires the explicit forms of the matrix elements involving the $P_{\psi s}^{\Lambda}$ state.

The relevant matrix elements are defined as follows:

$$\langle 0 | J_{\mu}(x) | P_{\psi s}^{\Lambda}(p_2, s) \rangle = \lambda_{P_{shs}^{\Lambda}} u_{\mu}(p_2, s),$$
 (8)

$$\langle P_{\psi s}^{\Lambda}(p_1, s) | \bar{J}_{\nu}(0) | 0 \rangle = \lambda_{P_{s h s}^{\Lambda}} \bar{u}_{\nu}(p_1, s),$$
 (9)

and the electromagnetic transition vertex is given by [56–59]:

$$\langle P_{\eta bs}^{\Lambda}(p_2, s) | P_{\eta bs}^{\Lambda}(p_1, s) \rangle_F = -e \,\bar{u}_{\mu}(p_2, s) \Gamma_{\mu\nu} u_{\nu}(p_1, s),$$
 (10)

with

$$\Gamma_{\mu\nu} = F_1(q^2) g_{\mu\nu} \not \xi - \frac{1}{2m_{P_{\eta/s}^{\Lambda}}} \left[F_2(q^2) g_{\mu\nu} \not \xi \not q + F_4(q^2) \frac{q_{\mu} q_{\nu} \not \xi \not q}{(2m_{P_{\eta/s}^{\Lambda}})^2} \right] + \frac{F_3(q^2)}{(2m_{P_{\eta/s}^{\Lambda}})^2} q_{\mu} q_{\nu} \not \xi, \tag{11}$$

where $\lambda_{P_{\psi s}^{\Lambda}}$ denotes the pole residue, u_{μ} is the Rarita-Schwinger spinor, ε is the photon polarization vector, and $F_{i}(q^{2})$ are the electromagnetic form factors.

Substituting Eqs. (7)–(11) into the correlation function and performing the necessary algebraic manipulations yields the final hadronic representation:

$$T_{\mu\nu}^{Had}(p,q) = \frac{\lambda_{P_{\psi s}^{\Lambda}}^{2}}{[(p+q)^{2} - m_{P_{\psi s}^{\Lambda}}^{2}][p^{2} - m_{P_{\psi s}^{\Lambda}}^{2}]} \left[2\varepsilon_{\mu}q_{\nu}\not q F_{1}(q^{2}) + 2q_{\mu}q_{\nu}\not q F_{2}(q^{2}) + \frac{F_{3}(q^{2})}{2m_{P_{\psi s}^{\Lambda}}}q_{\mu}q_{\nu}\not q \not q + \frac{F_{4}(q^{2})}{4m_{P_{\psi s}^{\Lambda}}^{3}}(\varepsilon.p)q_{\mu}q_{\nu}\not p \not q + 0 \right] + \text{ other independent structures}.$$

$$(12)$$

For clearer physical interpretation, the form factors $F_i(q^2)$ are related to the magnetic dipole (G_M) , electric quadrupole (G_Q) , and magnetic octupole (G_Q) form factors [56–59]:

$$G_{M}(q^{2}) = \left[F_{1}(q^{2}) + F_{2}(q^{2})\right] \left(1 + \frac{4}{5}\lambda\right) - \frac{2}{5} \left[F_{3}(q^{2}) + F_{4}(q^{2})\right] \lambda \left(1 + \lambda\right),$$

$$G_{Q}(q^{2}) = \left[F_{1}(q^{2}) - \lambda F_{2}(q^{2})\right] - \frac{1}{2} \left[F_{3}(q^{2}) - \lambda F_{4}(q^{2})\right] \left(1 + \lambda\right),$$

$$G_{O}(q^{2}) = \left[F_{1}(q^{2}) + F_{2}(q^{2})\right] - \frac{1}{2} \left[F_{3}(q^{2}) + F_{4}(q^{2})\right] \left(1 + \lambda\right),$$
(13)

where $\lambda = -\frac{q^2}{4m_{P_{abs}}^{2}}$. At $q^2 = 0$, these relations simplify to:

$$G_M(0) = F_1(0) + F_2(0),$$

$$G_Q(0) = F_1(0) - \frac{1}{2}F_3(0),$$

$$G_O(0) = F_1(0) + F_2(0) - \frac{1}{2}[F_3(0) + F_4(0)].$$
(14)

Since the present study focuses on the magnetic dipole, electric quadrupole, and magnetic octupole moments, these electromagnetic multipole moments are expressed in terms of the form factors introduced above. The magnetic dipole $(\mu_{P_{\psi_s}^{\Lambda}})$, electric quadrupole $(Q_{P_{\psi_s}^{\Lambda}})$, and magnetic octupole $(O_{P_{\psi_s}^{\Lambda}})$ moments can then be obtained from the corresponding form factors through the following procedure:

$$\mu_{P_{\psi s}^{\Lambda}} = G_M(0) \frac{e}{2m_{P^{\Lambda}}},\tag{15}$$

$$Q_{P_{\psi_s}^{\Lambda}} = G_Q(0) \frac{e^{\frac{e^{-\tau}}{m_{P_{\Lambda}}^{2}}}},$$
 (16)

$$O_{P_{\psi s}^{\Lambda}} = G_O(0) \frac{e}{2m_{P_{\eta h s}}^3}.$$
 (17)

From Ref. [60], it is observed that the masses of the $P_{\psi s}^{\Lambda}$ pentaquark states extracted from five different interpolating currents fall within a narrow region. In general, an interpolating current may couple to one or several hadronic states sharing the same quantum numbers, since such couplings are not prohibited by symmetries. Conversely, a hadron can contain multiple Fock components, each potentially coupling to a current with identical quantum numbers. These findings imply that a pentaquark state may accommodate different internal configurations, or that distinct pentaquark structures with similar masses coexist within the same mass region. If the mass splittings among these states are sizable, the expressions in Eqs. (7)–(15) apply to the lowest-mass state, and the magnetic dipole moments obtained from different interpolating currents are expected to converge. In contrast, if the masses are nearly degenerate, Eq. (7) yields a residue-squared-weighted average of the magnetic moments of the overlapping states. In the latter case, substantial differences between the intrinsic magnetic dipole moments of these nearly degenerate states will manifest as variations among the results obtained from different interpolating currents, reflecting their distinct coupling strengths to the physical configurations.

The QCD representation of the correlation function is derived by evaluating it in terms of quark and gluon degrees of freedom. This involves applying the operator product expansion (OPE) near the light-cone, which systematically incorporates both the perturbative and non-perturbative dynamics of the photon through its distribution amplitudes (DAs).

Applying Wick's theorem to contract the quark fields, the correlation function is expressed in terms of the relevant quark propagators. For the specific case of the J^1_{μ} interpolating current, we obtain the following explicit form:

$$T_{\mu\nu}^{QCD}(p,q) = -i \mathcal{A} \mathcal{A}' \int d^4x e^{ip \cdot x} \langle 0| \left\{ \text{Tr} \left[\gamma_5 S_s^{ee'}(x) \gamma_5 \widetilde{S}_u^{dd'T}(x) \right] \text{Tr} \left[\gamma_\mu S_c^{gg'}(x) \gamma_\nu \widetilde{S}_d^{ff'T}(x) \right] \right. \\ \left. + \text{Tr} \left[\gamma_5 S_s^{ee'}(x) \gamma_5 \widetilde{S}_d^{dd'T}(x) \right] \text{Tr} \left[\gamma_\mu S_c^{gg'}(x) \gamma_\nu \widetilde{S}_u^{ff'T}(x) \right] \right\} \left(\widetilde{S}_c^{c'cT}(-x) \right) |0\rangle_F,$$

$$(18)$$

where $\mathcal{A}\mathcal{A}' = \frac{1}{2} \, \varepsilon^{abc} \varepsilon^{a'b'c'} \varepsilon^{ade} \varepsilon^{a'd'e'} \varepsilon^{bfg} \varepsilon^{b'f'g'}$; and $\widetilde{S}^{ij}_{c(q)}(x) = C S^{ij\mathrm{T}}_{c(q)}(x) C$, with C and T being the charge conjugation and transpose of the operator, respectively.

In Eq. (18), $S_q(x)$ and $S_c(x)$ represent the light and charm quark propagators. Their explicit expressions are given by [61, 62]:

$$S_{q}(x) = \frac{1}{2\pi x^{2}} \left(i \frac{\cancel{x}}{x^{2}} - \frac{m_{q}}{2} \right) - i \frac{g_{s}}{16\pi^{2}x^{2}} \int_{0}^{1} dv \, G^{\mu\nu}(vx) \left[\bar{v} \cancel{x} \sigma_{\mu\nu} + v \sigma_{\mu\nu} \cancel{x} \right], \tag{19}$$

$$S_{c}(x) = \frac{m_{c}^{2}}{4\pi^{2}} \left[\frac{K_{1}(m_{c}\sqrt{-x^{2}})}{\sqrt{-x^{2}}} + i \frac{\cancel{x}}{K_{2}(m_{c}\sqrt{-x^{2}})} \right] - i \frac{m_{c} g_{s}}{16\pi^{2}} \int_{0}^{1} dv \, G^{\mu\nu}(vx) \left[\frac{K_{1}(m_{c}\sqrt{-x^{2}})}{\sqrt{-x^{2}}} (\sigma_{\mu\nu} \cancel{x} + \cancel{x} \sigma_{\mu\nu}) + 2\sigma_{\mu\nu} K_{0}(m_{c}\sqrt{-x^{2}}) \right], \tag{20}$$

where $G^{\mu\nu}(x)$ is the gluon field strength tensor, v is the line variable, and $K_n(m_c\sqrt{-x^2})$ are the Bessel functions. The photon's interaction with quarks is incorporated through two distinct mechanisms. The first involves a direct, perturbative coupling to a quark line. In this case, one of the free propagators in Eq. (18) is replaced by its counterpart that includes an electromagnetic interaction vertex:

$$S^{\text{free}}(x) \to \int d^4 z \, S^{\text{free}}(x-z) \mathcal{A}(z) \, S^{\text{free}}(z) \,. \tag{21}$$

Here, $S^{\text{free}}(x)$ corresponds to the leading term of the light and heavy quark propagators.

The second mechanism accounts for the non-perturbative coupling of the photon. This is described by substituting one of the light-quark propagators with a matrix element that encapsulates the photon's quark-antiquark structure:

$$S_{\mu\nu}^{ab}(x) \to -\frac{1}{4} \left[\bar{q}^a(x) \Gamma_i q^b(0) \right] \left(\Gamma_i \right)_{\mu\nu},\tag{22}$$

where $\Gamma_i = 1, \gamma_5, \gamma_\mu, i\gamma_5\gamma_\mu, \sigma_{\mu\nu}/2$. This substitution leads to matrix elements of the form $\langle \gamma(q)|\bar{q}(x)\Gamma_i q(0)|0\rangle$ and $\langle \gamma(q)|\bar{q}(x)\Gamma_i G_{\mu\nu}q(0)|0\rangle$, which are parameterized in terms of the photon DAs, following the established formalism [63]. By systematically implementing the substitutions from Eqs. (21) and (22), both the perturbative and non-perturbative photon interactions are fully incorporated into the QCD representation of the correlation function. The resulting expressions in coordinate space are then transformed to momentum space via a Fourier transformation, yielding the final form used for the subsequent QCD light-cone sum rule analysis.

Having obtained expressions for the correlation function at both the hadronic and quark-gluon levels, the next step involves deriving the sum rules for the electromagnetic multipole moments. The resulting analytical expressions for the magnetic dipole, electric quadrupole, and magnetic octupole moments of the $P_{\psi s}^{\Lambda}$ state, calculated using five different interpolating currents, are presented in the following equations:

$$\mu_{J_{\mu}^{i}} \lambda_{J_{\mu}^{i}}^{2} e^{-\frac{m_{J_{\mu}^{i}}^{2}}{M^{2}}} = \rho_{i}(M^{2}, s_{0}), \tag{23}$$

$$Q_{J_{i}^{i}} \lambda_{J_{i}^{i}}^{2} e^{-\frac{m_{J_{\mu}^{i}}^{2}}{M^{2}}} = \Delta_{i}(M^{2}, s_{0}), \tag{24}$$

$$\mathcal{O}_{J_{\mu}^{i}} \lambda_{J_{\mu}^{i}}^{2} e^{-\frac{m_{J_{\mu}^{i}}^{2}}{M^{2}}} = \Omega_{i}(M^{2}, s_{0}), \tag{25}$$

with i = 1, 2, ..., 5 labeling the five interpolating currents, where

$$\rho_i(M^2, s_0) = \frac{1}{2} \left[F_1^{J_\mu^i}(M^2, s_0) + F_2^{J_\mu^i}(M^2, s_0) \right], \tag{26}$$

$$\Delta_i(M^2, s_0) = \frac{1}{2} F_1^{J_\mu^i}(M^2, s_0) + m_{J_\mu^i} F_3^{J_\mu^i}(M^2, s_0), \tag{27}$$

$$\Omega_{i}(M^{2}, s_{0}) = \frac{1}{2} \left[F_{1}^{J_{\mu}^{i}}(M^{2}, s_{0}) + F_{2}^{J_{\mu}^{i}}(M^{2}, s_{0}) \right] + m_{J_{\mu}^{i}} F_{3}^{J_{\mu}^{i}}(M^{2}, s_{0}) + 2m_{J_{\mu}^{i}}^{2} F_{4}^{J_{\mu}^{i}}(M^{2}, s_{0}). \tag{28}$$

Given the extensive and structurally similar nature of the analytical results for the five currents, we provide the explicit expressions only for the first interpolating current, J^1_{μ} , in the Appendix as a representative example. The corresponding results for the other currents, J^2_{μ} to J^5_{μ} , are obtained analogously.

III. NUMERICAL ILLUSTRATIONS

This section is devoted to the numerical investigation of the QCD light-cone sum rule aimed at evaluating the electromagnetic multipole moments of the $P_{\psi s}^{\Lambda}$ state. In order to extract the magnetic dipole moment, several input parameters must be specified. The set of numerical inputs adopted in this study is summarized in Table I. For the numerical evaluation, the up and down quark masses are set to zero $(m_u = m_d = 0)$, while contributions proportional to m_s are retained. The photon DAs, along with their explicit expressions and the necessary numerical parameters, are adopted from Ref. [63]. In the present study, the calculations incorporate photon DAs up to twist-4 in order to account consistently for higher-twist effects.

Besides the previously mentioned input parameters, two additional quantities are necessary for the numerical evaluation: the continuum threshold, s_0 , and the Borel parameter, M^2 . In principle, the results should be independent of these parameters, but in practice, some dependence is unavoidable. Therefore, it is essential to determine a working region in which the numerical predictions exhibit minimal sensitivity to variations in s_0 and M^2 . The working region for the Borel parameter, M^2 , defined as the range over which the numerical results show minimal sensitivity to its variation, is determined by the constraints inherent to the adopted methodology. These constraints correspond to the pole contribution (PC) and the convergence of the operator product expansion (CVG). The definitions and

LE 1. IIIPut	parameters used in the numerical ana.
Inputs	Values
m_s	$93.5 \pm 0.8 \text{ MeV } [64]$
m_c	$1.273 \pm 0.0046 \text{ GeV } [64]$
$m_{J^1_\mu}$	$4.46 \pm 0.10 \text{ GeV } [60]$
$m_{J_{\mu}^2}$	$4.42 \pm 0.10 \text{ GeV } [60]$
$m_{J_{\mu}^3}$	$4.47 \pm 0.10 \text{ GeV } [60]$
$m_{J_{\mu}^4}^{^4}}$	$4.47 \pm 0.10 \text{ GeV } [60]$
$m_{J_{\mu}^5}$	$4.51 \pm 0.10 \text{ GeV } [60]$
$\lambda_{J^1_\mu}$	$(1.76 \pm 0.28) \times 10^{-3} \text{ GeV}^6 [60]$
$\lambda_{J^2_{\mu}}$	$(1.68 \pm 0.27) \times 10^{-3} \text{ GeV}^6 [60]$
$\lambda_{J^3_\mu}$	$(3.05 \pm 0.49) \times 10^{-3} \text{ GeV}^6 [60]$
$\lambda_{J_{\mu}^4}$	$(3.04 \pm 0.50) \times 10^{-3} \text{ GeV}^6 [60]$
$\lambda_{J_{\mu}^{5}}^{^{\mu}}$	$(1.87 \pm 0.30) \times 10^{-3} \text{ GeV}^6 [60]$
$\langle ar{q} q angle$	$(-0.24 \pm 0.01)^3 \text{ GeV}^3 [65]$
$\langle \bar{s}s \rangle$	$0.8 \times (-0.24 \pm 0.01)^3 \text{ GeV}^3 [65]$
$\langle g_s^2 G^2 \rangle$	$0.48 \pm 0.14 \text{ GeV}^4$ [66]
$f_{3\gamma}$	$-0.0039 \text{ GeV}^2 [63]$
χ	$-2.85 \pm 0.5 \text{ GeV}^{-2} [67]$

TABLE I. Input parameters used in the numerical analysis.

quantitative evaluation of these criteria are provided by the following expressions:

$$PC = \frac{\rho(M^2, s_0)}{\rho(M^2, \infty)} > 35\%, \tag{29}$$

$$PC = \frac{\rho(M^2, s_0)}{\rho(M^2, \infty)} > 35\%,$$

$$CVG = \frac{\rho^{\text{DimN}}(M^2, s_0)}{\rho(M^2, s_0)} < 5\%.$$
(29)

In this analysis, $\rho_i^{\text{DimN}}(M^2, s_0)$ denotes the highest-dimensional contributions in the operator product expansion of $\rho_i(M^2, s_0)$. Here, only the formalism corresponding to the magnetic dipole moment spectral density, $\rho_i(M^2, s_0)$, is explicitly presented. Similar analyses have also been performed for the electric quadrupole spectral density, $\Delta_i(M^2, s_0)$, and for the magnetic quadrupole spectral density, $\Omega_i(M^2, s_0)$. On the QCD side, the leading higher-order effects stem from the dimension-7 condensates $\langle g_s^2 G^2 \rangle \langle \bar{q}q \rangle$ and $\langle g_s^2 G^2 \rangle \langle \bar{s}s \rangle$. The CVG analysis is therefore performed by including these D7 terms, and the parameters reported in Table II are obtained within this setup. The QCD representation further involves several operator structures of lower dimensionalities, such as $\langle g_s^2 G^2 \rangle f_{3\gamma}$ (D6), $\langle g_s^2 G^2 \rangle \langle \bar{q}q \rangle \chi$ and $\langle g_s^2 G^2 \rangle \langle \bar{s}s \rangle \chi$ (D5), $\langle \bar{q}q \rangle$ and $\langle \bar{s}s \rangle$ (D3), $f_{3\gamma}$ (D2), and $\langle \bar{q}q \rangle \chi$ and $\langle \bar{s}s \rangle \chi$ (D1). Once these conditions were satisfied, we proceeded with confidence in the robustness of our predictions. Figure 2 presents the results specifically for the magnetic dipole moment, demonstrating that within the selected Borel window, the PC remains substantially larger than the continuum contribution, ensuring the dominance of the ground state. Simultaneously, the relative sizes of the condensate terms indicate a satisfactory CVG. For completeness, Fig. 2 also shows the dependence of the $P_{\psi s}^{\Lambda}$ magnetic dipole moment on the Borel parameter M² and the continuum threshold s₀. As expected, only mild variations are observed within the chosen ranges, although a residual sensitivity to these parameters persists, contributing to the overall uncertainty.

With all the necessary input parameters and auxiliary quantities, such as the continuum threshold s₀ and the Borel parameter M², determined, we now present the resulting numerical values. The complete set of results, including the estimated uncertainties arising from the intrinsic variability of the input parameters, is summarized in Table III.

As presented in Table III, the magnetic dipole moments of the $P_{\psi s}^{\Lambda}$ pentaquark, evaluated using several distinct interpolating currents but sharing the same quark content, display noticeable variations. This behavior may indicate the presence of more than one $P_{\psi s}^{\Lambda}$ -type pentaquark state (see the discussion following Eq. (15)), characterized by identical quantum numbers and similar quark configurations, yet differing in their electromagnetic properties. As discussed earlier, the employed interpolating currents share the same quantum numbers and consequently lead to nearly degenerate mass predictions for the $P_{\psi s}^{\Lambda}$ states [60]. Nevertheless, the extracted magnetic dipole, electric quadrupole and magnetic octupole moments exhibit a pronounced dependence on the internal diquark–diquark– antiquark organization and the microscopic structure of the considered state. Although it is often assumed and

State	$s_0 (GeV^2)$	$M^2 (GeV^2)$	CVG (%)	PC (%)
J^1_μ	[26.0, 28.0]	[2.5, 3.1]	[0.10, 0.12]	[66.18, 42.54]
J_{μ}^2	[26.0, 28.0]	[2.7, 3.3]	[0.09, 0.13]	[68.18, 47.20]
J_{μ}^3	[26.0, 28.0]	[2.5, 3.1]	[0.10, 0.13]	[63.88, 40.45]
J_{μ}^4	[26.0, 28.0]	[2.5, 3.1]	[0.15, 0.18]	[67.37, 43.18]
J_{μ}^{5}	[26.0, 28.0]	[2.5, 3.1]	[0.10, 0.14]	[67.60, 43.83]

TABLE III. Numerical results of the magnetic dipole (in units of μ_N), electric quadrupole (in units of 10^{-2} fm²) and magnetic octupole (in units of 10^{-2} fm³) moments of the $P_{\psi_S}^{\Lambda}$.

State	$\mu_{P_{\psi s}^{\Lambda}}$	$\mathcal{Q}_{P_{\psi s}^{\Lambda}}$	$\mathcal{O}_{P_{\psi s}^{\Lambda}}$
J^1_μ	-2.28 ± 0.57	-0.90 ± 0.18	-0.49 ± 0.10
J_{μ}^2	-0.15 ± 0.04	-1.44 ± 0.29	-1.02 ± 0.21
J_{μ}^{3}	1.60 ± 0.40	0.24 ± 0.05	-0.13 ± 0.03
J_{μ}^4	-1.26 ± 0.32	3.17 ± 0.64	1.44 ± 0.30
J_{μ}^{5}	3.36 ± 0.84	-2.32 ± 0.47	-1.88 ± 0.38

expected that a change in the hadronic basis does not alter physical observables, this assumption may not hold for quantities directly linked to internal dynamics, such as magnetic dipole moments. Since these observables are highly sensitive to the spatial and spin configurations of the constituent quarks, a transformation of the interpolating basis effectively modifies the internal structure of the state, which can, in turn, lead to substantial variations in the computed electromagnetic multipole moments. Indeed, several studies [40, 47, 68–70] employing different types of interpolating currents have reported significant differences in the magnetic dipole moments of multi-quark systems. These findings collectively suggest that variations in the choice of interpolating currents, as well as in the isospin or charge configurations of the investigated states, can yield distinct magnetic dipole moments even for hadrons with the same quark content.

As seen from Table III, the higher electromagnetic multipole moments, similar to the magnetic dipole moment, exhibit a strong dependence on the specific diquark–diquark–antiquark configuration adopted for the $P_{\psi s}^{\Lambda}$ pentaquark. The magnitudes of the electric quadrupole and magnetic octupole moments are considerably smaller than that of the magnetic dipole moment, yet their nonvanishing values clearly indicate a nonspherical charge distribution. The relative magnitudes and signs of these higher moments provide insight into the deformation and orientation of the underlying hadronic structure. For the interpolating currents J_{μ}^{1} , J_{μ}^{2} , and J_{μ}^{5} , both the electric quadrupole and magnetic octupole moments are negative, suggesting an oblate deformation, where the charge distribution is flattened along the symmetry axis. In contrast, the J_{μ}^{3} and J_{μ}^{4} currents yield positive values for the quadrupole moments—implying a prolate deformation, in which the charge distribution is elongated along the symmetry axis. Moreover, for J_{μ}^{3} , the opposite signs of the quadrupole and octupole moments (positive and negative, respectively) indicate that the charge and geometric distributions are oriented differently. These results suggest that the multipole structure of the $P_{\psi s}^{\Lambda}$ pentaquark is highly sensitive to the underlying diquark configuration encoded in the interpolating current.

Such sensitivity may provide a useful probe for distinguishing between different internal diquark–diquark–antiquark configurations in future experimental or lattice studies.

To gain a deeper understanding of the observed variations in the results, we have analyzed the contributions of individual quarks, with the corresponding findings summarized in Tables IV–VI. This can be attained by choosing the relevant charge factors e_u , e_d , e_s , and e_c . These results are evaluated using the central values of all input parameters. The individual quark contributions to the magnetic dipole, electric quadrupole, and magnetic octupole moments of the $P_{\psi s}^{\Lambda}$ pentaquark reveal several interesting features. For the magnetic dipole moment, the up and down quarks provide the dominant contributions, often with opposite signs that partially cancel each other. The strange and charm quarks generally contribute less, although their effects become more pronounced in certain interpolating currents, such as J_{μ}^2 and J_{μ}^3 . In the case of the electric quadrupole moments, the charm quark contributions are substantial in most currents, highlighting its influence on the deformation of the charge distribution. Notably, the J_{μ}^4 current exhibits large positive contributions from all quarks, leading to a strongly positive total quadrupole moment, consistent with a prolate deformation. Conversely, for J_{μ}^1 , J_{μ}^2 , and J_{μ}^5 , the combined contributions produce negative total quadrupole moments, indicative of an oblate geometry. The magnetic octupole moments show similar trends. The up and down quarks largely dominate, with partial cancellations shaping the total value, while the strange and charm quarks provide moderate corrections. The interplay of contributions from all quarks results in both positive and negative total octupole moments across different interpolating currents, reflecting the sensitivity of the octupole structure to the internal quark configuration. Overall, these findings underline that the electromagnetic multipole moments of the $P_{\psi s}^{\Lambda}$ are highly sensitive to the underlying quark arrangement, and different interpolating currents probe distinct str

To dissect the microscopic mechanisms behind the structural deformations, we decompose the electric quadrupole and magnetic octupole moments into individual quark contributions, as shown in Figs. 3-4. This decomposition uncovers several critical insights. First, regarding the quadrupole deformation, the charm quark emerges as the principal actor. Its substantial negative contribution in oblate configurations (e.g., J^1_{μ} , J^2_{μ} , J^5_{μ}) and positive contribution in prolate ones (e.g., J_{μ}^{3} , J_{μ}^{4}) indicate that the spatial distribution of the heavy charm quark is a major factor in the system's elongation or flattening. This dominance can be understood by considering the large mass of the charm quark, which, in the spirit of heavy-quark effective theory, suggests that the lighter degrees of freedom adjust their dynamics around it, thereby making the charm quark's distribution a primary driver of the collective deformation. Second, we observe a complex interplay for the magnetic octupole moment. While light quarks provide the largest individual contributions, they frequently exhibit partial cancellation (e.g., the up and down quark contributions often oppose each other). The net octupole moment is then often determined by the smaller, yet uncompensated, contributions from the strange and charm quarks. This reveals that the higher-order magnetic structure is exceptionally sensitive to minor asymmetries in the strange-charm sector, acting as a magnifying glass for subtle flavor-dependent dynamics. Collectively, these results provide a structural fingerprint for each configuration. For example, a future experimental observation of a large oblate deformation would strongly suggest a configuration where the charm quark's wavefunction is concentrated in the equatorial plane, as seen in our J_{μ}^{5} current. Most importantly, this flavor decomposition maps abstract multipole moments directly onto specific quark-level behaviors, transforming them from gross structural indicators into precise diagnostic tools for benchmarking theoretical models against future experimental data.

TABLE IV. Individual quark contributions to the magnetic dipole moments (in units of μ_N).

State	μ_u	μ_d	μ_s	μ_c	μ_{tot}
J^1_{μ}	-3.52	1.76	~ 0	-0.52	-2.28
J_{μ}^{2}	-3.62	1.81	3.62	-1.96	-0.15
J_{μ}^3	-8.82	4.41	4.71	1.30	1.60
J_{μ}^4	-9.34	2.24	3.94	1.90	-1.26
J_{μ}^{5}	~ 0	~ 0	3.80	-0.44	3.36

A critical test for the structural interpretations of the $P_{\psi s}^{\Lambda}$ state is provided by comparing its predicted magnetic

TABLE V. Individual quark contributions to the electric quadrupole moments ($\times 10^{-2}$ in units of fm²).

State	\mathcal{Q}_u	\mathcal{Q}_d	\mathcal{Q}_s	\mathcal{Q}_c	\mathcal{Q}_{tot}
J^1_μ	0.84	-0.42	~ 0	-1.32	-0.90
J_{μ}^2	0.88	-0.44	-0.80	1.00	-1.44
J_{μ}^3	0.06	-0.03	-1.10	1.31	0.24
J_{μ}^4	0.06	0.55	1.18	1.38	3.17
J_{μ}^{5}	~ 0	~ 0	-0.89	-1.43	-2.32

TABLE VI. Individual quark contributions to magnetic octupole moments ($\times 10^{-2}$ in units of fm³).

State	\mathcal{O}_u	\mathcal{O}_d	\mathcal{O}_s	\mathcal{O}_c	\mathcal{O}_{tot}
J^1_μ	0.82	-0.41	~ 0	-0.90	-0.49
J_{μ}^2	0.86	-0.43	-0.86	-0.59	-1.02
J_{μ}^{3}	1.52	-0.76	-1.11	0.22	-0.13
J_{μ}^4	1.52	-0.18	-0.27	0.37	1.44
J_{μ}^{5}	~ 0	~ 0	-0.88	-1.00	-1.88

dipole moment across different theoretical frameworks, all assuming $J^P=\frac{3}{2}^-$. Our results, summarized in Table III for the compact pentaquark picture, reveal a spectrum of values that is both wide and informative. This diversity stands in stark contrast to existing literature. Calculations based on a molecular configuration yield values of $\mu_{P^{\Lambda}} = 0.465 \ \mu_N$ (quark model) [33], $\mu_{P_{\psi s}^{\Lambda}} = -0.231~\mu_N$ [37] (quark model) and $\mu_{P_{\psi s}^{\Lambda}} = -1.67 \pm 0.58~\mu_N$ (QCD light-cone sum rules) [36]. Notably, our predictions for the compact state not only differ in magnitude from these molecular results but also span both positive and negative signs, a direct consequence of the distinct interpolating currents employed. This pronounced model-dependence is, in fact, a key strength of the magnetic moment as an observable. The large variation in our predictions for different currents means that a future experimental measurement of the magnetic moment will not merely provide a number, but will act as a powerful discriminator. It will allow us to rule out entire classes of interpolating currents and, by extension, the specific internal configurations they represent, thereby providing a stringent test for our theoretical understanding of the pentaquark's structure. The discrepancies between our compact pentaquark results and the molecular predictions from other studies highlight the pivotal role of the magnetic moment in discriminating between core structural models. The underlying reasons for the spread are multifaceted, stemming from fundamental differences in the assumed spatial organization of quarks (compact vs. loose molecule), the choice of dynamical framework (QCD sum rules vs. quark models), and the associated parameterizations. In conclusion, while the precise value remains model-dependent, our analysis firmly establishes the magnetic dipole moment as a powerful diagnostic tool. The substantial differences observed between various structural assumptions suggest that future, more precise experimental constraints on this quantity could be decisive in elucidating the true nature of the $P_{\psi s}^{\Lambda}$ pentaquark.

IV. STRUCTURAL INTERPRETATION AND EXPERIMENTAL SIGNATURES

The pronounced variations in the electromagnetic moments across the five interpolating currents, despite their shared quantum numbers $J^P = \frac{3}{2}^-$, indicate a high sensitivity to the internal quark-gluon organization. This diversity suggests that the $P_{\psi s}^{\Lambda}$ spectrum may host multiple near-degenerate states or that a single state admits several distinct structural configurations. Below, we interpret our results and provide specific experimental signatures to discriminate between these possibilities.

A. Structural Interpretation of the Currents

The five currents employed in this study can be grouped into distinct structural categories based on their diquark content and Lorentz architecture:

- J_{μ}^{3} and J_{μ}^{4} : Compact Axial-Vector Dominated Configurations. These currents, built from two axial-vector diquarks, are optimized to probe compact multiquark cores. The positive quadrupole moment of J_{μ}^{4} (Q = 3.17) signals a prolate charge distribution, characteristic of a tightly-bound, anisotropic system. The significant magnetic moments arise from the aligned spins in the axial-vector diquarks.
- J^1_{μ} and J^2_{μ} : Scalar-diquark dominated configurations. These currents contain substantial scalar diquark components $(C\gamma_5)$, which are energetically favored in one-gluon exchange and couple strongly to compact configurations. However, through Fierz rearrangement, the same scalar diquark structure may also overlap with molecular-type components such as $\bar{D}^{(*)}\Xi_c$, where the light-quark subsystem forms a scalar correlation. The consistently negative quadrupole moments (Q < 0) indicate an oblate deformation, consistent with either compact scalar clustering or peripheral charge distributions in loosely bound molecular configurations.
- J_{μ}^{5} : Sector-Separated Cluster. This current uniquely isolates a non-strange scalar diquark [ud] from an axial-vector strange-charm diquark [sc]. This clear flavor-spin separation leads to the largest predicted magnetic moment ($\mu = 3.36 \ \mu_N$) and a strong oblate deformation ($\mathcal{Q} = -2.32$), serving as a unique fingerprint for this specific clustering pattern.

TABLE VII. Theoretical benchmarks for experimental discrimination of the $P_{\psi s}^{\Lambda}$ structure. The photon angular distribution, $W(\theta_{\gamma})$, refers to the $P_{\psi s}^{\Lambda} \to J/\psi \Lambda \gamma$ decay in the $P_{\psi s}^{\Lambda}$ rest frame, where θ_{γ} is the angle between the photon momentum and the spin-quantization axis of the $P_{\psi s}^{\Lambda}$.

Current	$\mu \; (\mu_N)$	$\mathcal{Q} \; (10^{-2} \; \mathrm{fm}^2)$	Experimental Signature
J^1_μ	-2.28 ± 0.57	-0.90 ± 0.18	Moderate rate. Broad, $\sin^2\!\theta_{\gamma}$ -dominated distribution with oblate distortion.
J_{μ}^{2}	-0.15 ± 0.04	-1.44 ± 0.29	Highly suppressed rate. Strongly $\cos^2\!\theta_\gamma\text{-dominated}$ distribution.
J_{μ}^{3}	1.60 ± 0.40	0.24 ± 0.05	Significant rate. Nearly pure dipolar $(\sin^2 \theta_{\gamma})$ distribution.
J_{μ}^4	-1.26 ± 0.32	3.17 ± 0.64	Significant rate. Strongly $\cos^2\theta_{\gamma}$ -dominated, sharp peak at poles.
J_{μ}^{5}	3.36 ± 0.84	-2.32 ± 0.47	Largest rate. $\sin^2 \theta_{\gamma}$ base with significant equatorial enhancement.

B. Experimental Discriminators and Future Measurements

The most direct experimental probe of the electromagnetic structure of the $P_{\psi s}^{\Lambda}$ states is through their radiative decays, accessible in processes like $\Xi_b^- \to J/\psi \Lambda K^- \gamma$ at LHCb and Belle II. The key observables are the radiative

decay width (proportional to $|G_M(0)|^2$) and the photon angular distribution, which is highly sensitive to the ratio G_Q/G_M .

In Table VII, we provide a set of theoretical benchmarks that directly connect our predictions to measurable quantities. The angular distribution of the photon in the $P_{\psi s}^{\Lambda}$ rest frame, $W(\theta_{\gamma})$, can be parameterized in terms of the multipole ratios, providing a direct experimental handle on the underlying deformation.

The following are decisive experimental scenarios:

- A measurement of a large radiative branching fraction combined with a photon angular distribution strongly peaked along the spin axis (large positive G_Q/G_M) would be a smoking gun for the prolate, compact configuration of J_{μ}^4 .
- Conversely, a large magnetic moment ($\mu \gtrsim 3\mu_N$) together with a flattened, oblate angular distribution would provide compelling evidence for the sector-separated structure of J_{μ}^5 .
- A highly suppressed radiative decay would point towards the J_{μ}^2 -like configuration, where the internal currents largely cancel.

Although the extraction of the multipole moments is experimentally challenging, the predicted angular and polarization patterns can, in principle, be resolved in high-statistics analyses of $\Xi_b^- \to J/\psi \Lambda K^- \gamma$ decays. Such analyses are within reach of current amplitude reconstruction techniques at LHCb. The correlations between the photon emission angle and the spin alignment of the $P_{\psi s}^{\Lambda}$, as established in this study, provide a framework that is largely independent of the specific current choice. Therefore, the present results provide a realistic theoretical basis for future LHCb and Belle II measurements aimed at mapping the electromagnetic geometry of hidden-charm strange pentaquarks.

In addition to experimental efforts, lattice QCD provides a complementary and first-principles framework for investigating the electromagnetic structure of multiquark systems. Although current lattice simulations of hidden-charm pentaquarks remain challenging due to their high masses and multi-hadron nature, recent progress in computing electromagnetic form factors of doubly charmed baryons [71, 72] and doubly bottom tetraquark [73] suggests that analogous calculations for pentaquarks may soon become feasible. Such lattice studies would offer a valuable cross-check of our predictions for the magnetic dipole, electric quadrupole, and magnetic octupole moments, thereby providing an ab initio benchmark for the nonperturbative dynamics captured by QCD sum rules.

V. SUMMARY AND CONCLUSIONS

In this work, we have performed a comprehensive analysis of the electromagnetic properties of the hidden-charm strange pentaquark with $J^P=3/2^-$ within the framework of QCD light-cone sum rules. Employing five distinct diquark-diquark-antiquark interpolating currents, we have calculated the magnetic dipole, electric quadrupole, and magnetic octupole moments to probe the internal structure of this exotic state.

Our main findings can be summarized as follows:

- The electromagnetic multipole moments exhibit strong sensitivity to the choice of interpolating current, demonstrating their intimate connection to the internal quark-gluon structure of the pentaquark.
- Magnetic dipole moments range from $-2.28 \,\mu_N$ to $+3.36 \,\mu_N$, establishing μ as a powerful discriminator among different internal configurations with identical quantum numbers.
- Non-zero electric quadrupole and magnetic octupole moments indicate a non-spherical charge distribution, with the sign and magnitude of these moments revealing a complex pattern of prolate and oblate deformations across different currents.
- Flavor decomposition shows that light quarks dominate the magnetic dipole response, often with significant cancellations, whereas the charm quark significantly influences the quadrupole deformation.

The systematic variation across five distinct currents provides a structural map of the pentaquark configuration space. As detailed in Section IV, we have provided specific structural interpretations for each current and established experimental benchmarks (Table VII) that connect our theoretical predictions to measurable quantities in radiative decays. Our predictions provide essential benchmarks for future experimental investigations—such as analyses of $\Xi_b^- \to J/\psi \Lambda K^- \gamma$ at LHCb and Belle II—as well as for complementary lattice QCD studies. These efforts will be crucial for unveiling the true nature of these enigmatic pentaquark states and guiding the interpretation of forthcoming experimental data. This multi-current approach establishes a new paradigm for exotic hadron spectroscopy, moving beyond mass-based classification to structure-sensitive observables that directly probe QCD's non-perturbative dynamics.

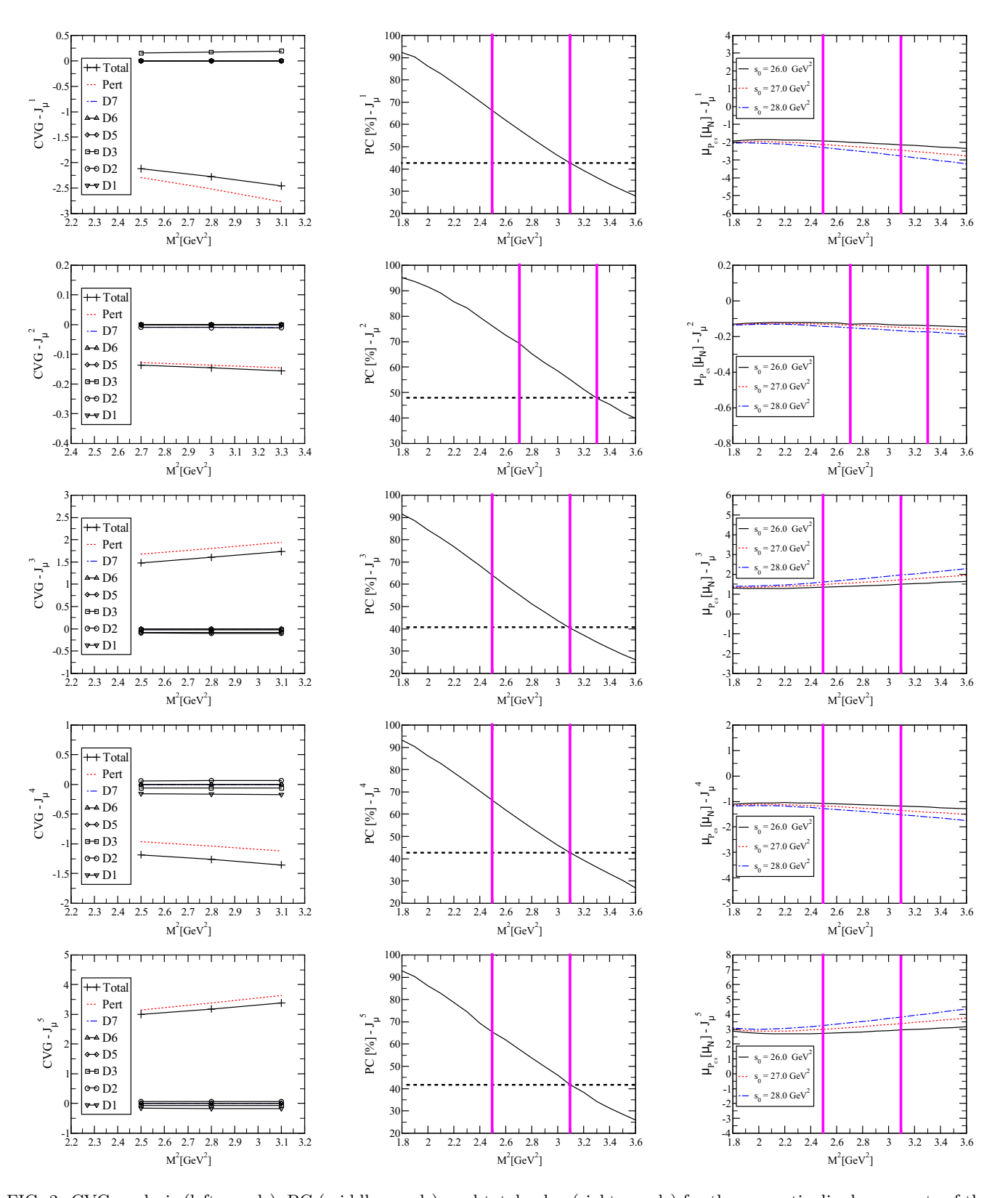


FIG. 2. CVG analysis (left panels), PC (middle panels), and total value (right panels) for the magnetic dipole moments of the $P_{\psi s}^{\Lambda}$ pentaquarks versus M^2 at fixed s_0 values. The adopted Borel window is illustrated by the vertical lines in the middle and right panels, whereas the horizontal line in the middle panel marks the minimum PC value obtained within this region.

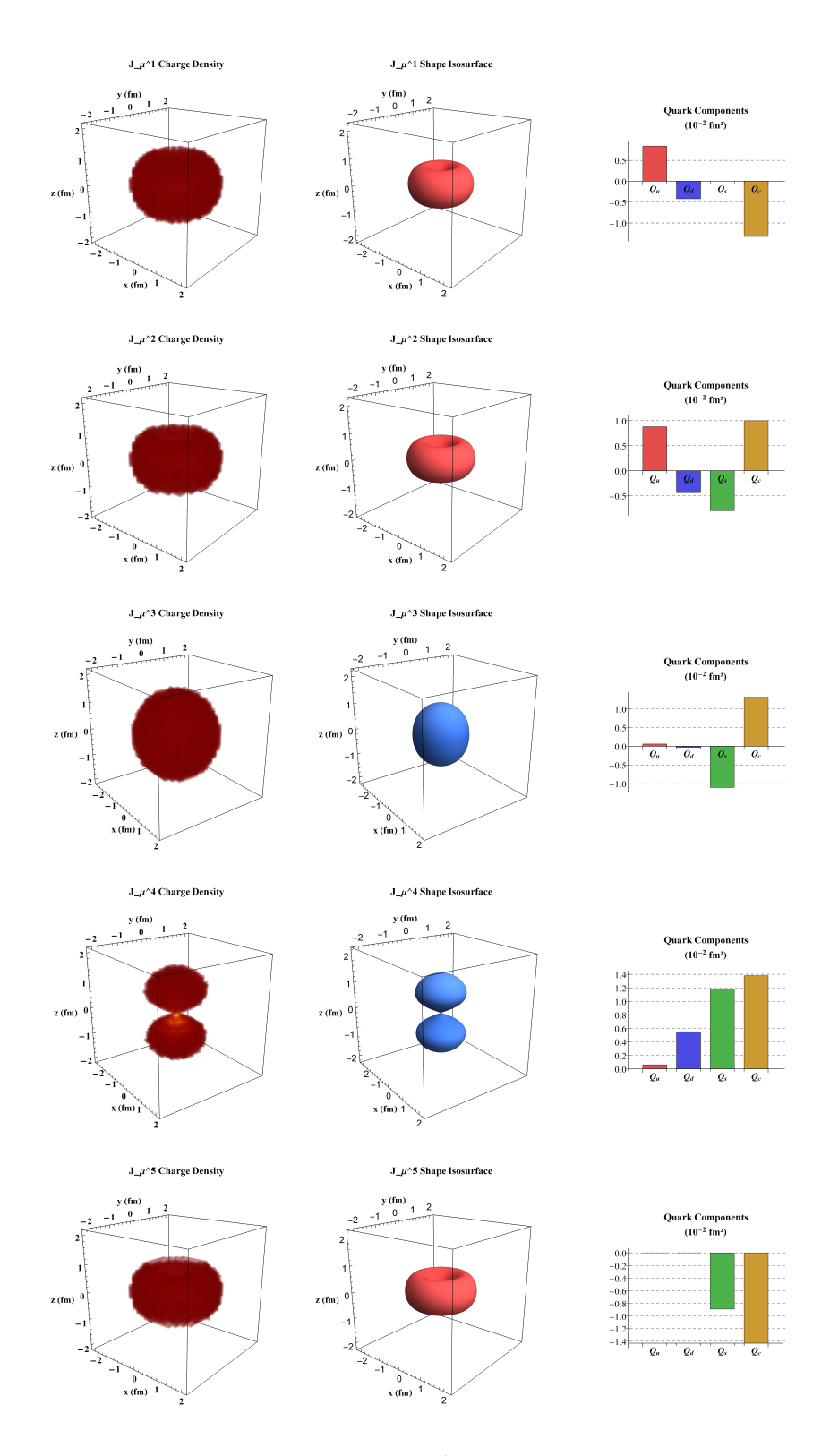


FIG. 3. Analysis of the electric quadrupole moment for the $P_{\psi s}^{\Lambda}$ pentaquark states. Left: three-dimensional charge density distribution ρ (e/fm³); Middle: isosurface visualization at 15% of maximum density showing deformation patterns; Right: individual quark contributions to the quadrupole moment (fm²). The plots reveal distinct prolate/oblate deformations characteristic of each pentaquark configuration, with color coding indicating density intensity. All spatial axes are in femtometers (fm).

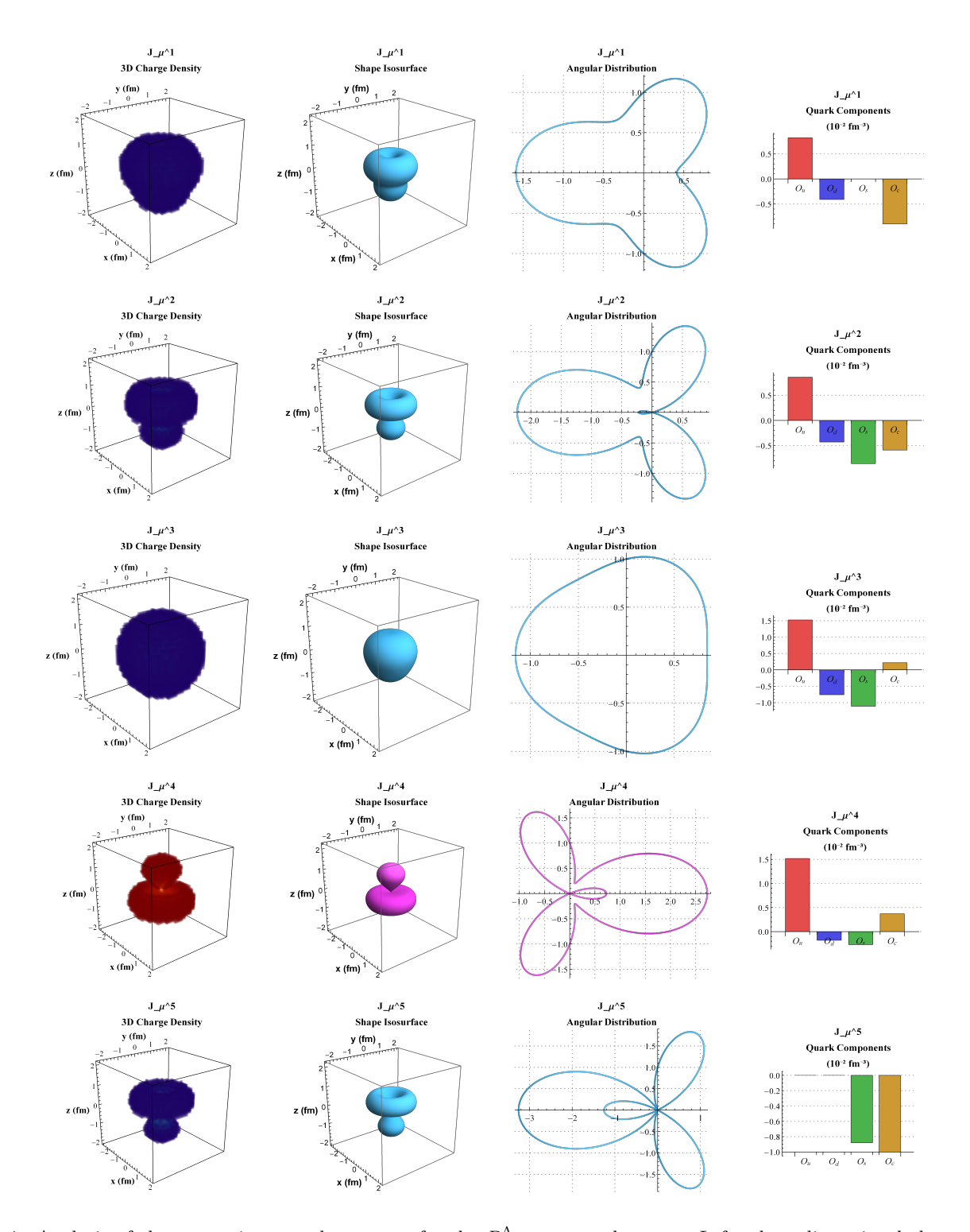


FIG. 4. Analysis of the magnetic octupole moment for the $P_{\psi s}^{\Lambda}$ pentaquark states. Left: three-dimensional charge density distribution ρ (e/fm³) exhibiting octupole deformation patterns; Middle left: isosurface visualization at 15% of maximum density, clearly displaying the characteristic peanut shape (positive octupole) or butterfly shape (negative octupole); Middle right: angular distribution of charge density showing the $Y_{30} \propto (5\cos^3\theta - 3\cos\theta)$ spherical harmonic dependence; Right: quark-sector decomposition of octupole moment components (×10⁻² fm³). Positive octupole moments indicate axial charge accumulation (peanut shape), while negative moments show equatorial charge concentration with polar depletion (butterfly shape). The angular distributions reveal the underlying octupole symmetry. All spatial axes are in femtometers (fm).

APPENDIX: EXPLICIT FORM OF THE ANALYTICAL RESULTS FOR THE ELECTROMAGNETIC MULTIPOLE MOMENTS OF THE J^1_μ CURRENT

In this appendix, we present the explicit analytical expressions for the magnetic dipole, electric quadrupole, and magnetic octupole moments derived for the J^1_μ interpolating current. These expressions are obtained after performing the full QCD-side calculation and matching it to the corresponding hadronic representation within the framework of light-cone QCD sum rules. Each multipole moment is expressed in terms of the relevant invariant amplitudes, Borel parameters, and distribution amplitudes, which encode the internal electromagnetic structure of the considered state. The final analytical results are given as follows:

$$\mu_{J_{\mu}^{1}} \lambda_{J_{\mu}^{1}}^{2} e^{-\frac{m_{J_{\mu}^{1}}^{2}}{M^{2}}} = \rho_{1}(M^{2}, s_{0}), \tag{31}$$

$$Q_{J_{\mu}^{1}} \lambda_{J_{\mu}^{1}}^{2} e^{-\frac{m_{J_{\mu}^{1}}^{2}}{M^{2}}} = \Delta_{1}(M^{2}, s_{0}), \tag{32}$$

$$\mathcal{O}_{J_{\mu}^{1}} \lambda_{J_{\mu}^{1}}^{2} e^{-\frac{m_{J_{\mu}^{1}}^{2}}{M^{2}}} = \Omega_{1}(M^{2}, s_{0}), \tag{33}$$

where,

$$\rho_1(\mathbf{M}^2, \mathbf{s}_0) = \frac{1}{2} \left[F_1^{J_\mu^1}(\mathbf{M}^2, \mathbf{s}_0) + F_2^{J_\mu^1}(\mathbf{M}^2, \mathbf{s}_0) \right], \tag{34}$$

$$\Delta_1(\mathbf{M}^2, \mathbf{s}_0) = \left[\frac{1}{2} F_1^{J_\mu^1}(\mathbf{M}^2, \mathbf{s}_0) + m_{J_\mu^1} F_3^{J_\mu^1}(\mathbf{M}^2, \mathbf{s}_0) \right], \tag{35}$$

$$\Omega_{1}(\mathbf{M}^{2}, \mathbf{s}_{0}) = \left[\frac{1}{2}F_{1}^{J_{\mu}^{1}}(\mathbf{M}^{2}, \mathbf{s}_{0}) + \frac{1}{2}F_{2}^{J_{\mu}^{1}}(\mathbf{M}^{2}, \mathbf{s}_{0}) + m_{J_{\mu}^{1}}F_{3}^{J_{\mu}^{1}}(\mathbf{M}^{2}, \mathbf{s}_{0}) + 2m_{J_{\mu}^{1}}^{2}F_{4}^{J_{\mu}^{1}}(\mathbf{M}^{2}, \mathbf{s}_{0})\right],\tag{36}$$

with

$$\begin{split} F_{1}^{J_{\mu}^{1}}(\mathbf{M}^{2},\mathbf{s}_{0}) &= \frac{1}{2^{28}\times3\times5^{3}\times7^{2}\pi^{7}} \Big[(218e_{c} - 621(e_{d} + e_{u}))I[0,7] + (378e_{c} - 1113(e_{d} + e_{u}))I[1,6] \Big] \\ &+ \frac{\langle g_{s}^{2}G^{2}\rangle\langle\bar{q}q\rangle}{2^{28}\times3^{6}\times5\pi^{5}} \Big[\Big(-160(e_{d} + e_{u})m_{c}\mathbb{A}[u_{0}] - 99e_{u}m_{s}I_{1}[\mathcal{S}] - 342e_{u}m_{s}I_{3}[\mathcal{S}] + 828((e_{d} + e_{u})m_{c} - e_{d}m_{s})(3I_{3}[\mathcal{T}_{1}] + 2(I_{3}[\mathcal{T}_{2}] + I_{3}[\mathcal{T}_{4}])) \Big)I[0,3] + 64\chi(e_{d} + e_{u})m_{c}I[0,4]\varphi_{\gamma}[u_{0}] \Big] \\ &+ \frac{11\langle g_{s}^{2}G^{2}\rangle f_{3\gamma}}{2^{31}\times3^{6}\times5\pi^{5}} \Big[891(2e_{s} + e_{u})I_{1}[\mathcal{A}] + 792(2e_{s} + e_{u})I_{1}[\mathcal{V}] + 1782e_{s}I_{3}[\mathcal{A}] + 2961e_{u}I_{3}[\mathcal{A}] - 1584e_{s}I_{3}[\mathcal{V}] \\ &- 2862e_{u}I_{3}[\mathcal{V}] - 144e_{u}I_{5}[\psi^{a}] - 504e_{s}\psi^{a}[u_{0}] - 152e_{u}\psi^{a}[u_{0}] + 104e_{u}\psi_{\gamma}^{\nu}[u_{0}] + 2e_{d}(1863I_{3}[\mathcal{A}] - 1863I_{3}[\mathcal{V}] \\ &- 252I_{5}[\psi^{a}] + 5\psi^{a}[u_{0}] + 178\psi_{\gamma}^{\nu}[u_{0}]) \Big] \\ &+ \frac{\langle \bar{q}q\rangle}{2^{25}\times3\times5^{2}\pi^{5}} \Big[\Big(-5e_{u}m_{s}I_{3}[\mathcal{S}] + 2(2(e_{d} + e_{u})m_{c} - 5e_{d}m_{s})(3I_{3}[\mathcal{T}_{1}] + 2(I_{3}[\mathcal{T}_{2}] + I_{3}[\mathcal{T}_{4}])) \Big)I[0,5] \Big] \\ &+ \frac{f_{3\gamma}}{2^{26}\times3^{2}\times5\pi^{5}} \Big[(2e_{d} + e_{u})(I_{3}[\mathcal{A}] - I_{3}[\mathcal{V}])I[0,6] \Big], \end{split}$$

$$F_{2}^{J_{\mu}^{1}}(M^{2}, s_{0}) = -\frac{9e_{c}}{2^{26} \times 5^{3} \times 7\pi^{7}} I[1, 6]$$

$$+ \frac{\langle g_{s}^{2} G^{2} \rangle \langle \bar{q}q \rangle}{2^{26} \times 3^{6} \times 5\pi^{5}} \Big[\Big(80(e_{d} + e_{u}) m_{c} \mathbb{A}[u_{0}] + 9e_{u} m_{s} (13I_{1}[S] - 11I_{3}[S]) \Big) I[0, 3] - 32\chi(e_{d} + e_{u})$$

$$\times m_{c} I[0, 4] \varphi_{\gamma}[u_{0}] \Big]$$

$$+ \frac{\langle g_{s}^{2} G^{2} \rangle f_{3\gamma}}{2^{31} \times 3^{5} \times 5\pi^{5}} \Big[\Big(69(36e_{d} - 14e_{s} + 13e_{u})I_{1}[\mathcal{V}] - 12(207e_{d} - 58e_{s} + 86e_{u})I_{3}[\mathcal{V}] + 48(14e_{d} + 10e_{s} + 9e_{u})I_{5}[\psi^{a}] - 4(61e_{d} + 34e_{u})\psi^{a}[u_{0}] \Big) I[0, 4] \Big]$$

$$+ \frac{e_{u} m_{s} \langle \bar{q}q \rangle}{2^{26} \times 3 \times 5\pi^{5}} I_{1}[S] I[0, 5]$$

$$+ \frac{f_{3\gamma}}{2^{28} \times 3^{3} \times 5\pi^{5}} \Big[\Big((48e_{d} + 2e_{s} + 25e_{u})I_{1}[\mathcal{V}] - 4(12e_{d} + 2e_{s} + 7e_{u})I_{3}[\mathcal{V}] \Big) I[0, 6] \Big], \tag{38}$$

$$F_{3}^{J_{\mu}^{1}}(M^{2}, s_{0}) = \frac{191 e_{c} m_{c}}{2^{25} \times 3^{2} \times 5^{3} \times 7\pi^{7}} I[0, 6]$$

$$+ \frac{\langle g_{s}^{2} G^{2} \rangle \langle \bar{q}q \rangle}{2^{26} \times 3^{6} \times 5\pi^{5}} \Big[e_{u} m_{c} m_{s} I_{3}[\mathcal{S}] I[0, 2] \Big]$$

$$+ \frac{\langle g_{s}^{2} G^{2} \rangle f_{3\gamma} m_{c}}{2^{29} \times 3^{4} \times 5\pi^{5}} \Big[\Big((187 e_{d} - 40 e_{s} + 112 e_{u}) I_{1}[\mathcal{V}] - 30(55 e_{d} + 28 e_{u}) I_{3}[\mathcal{V}] - 2(2 e_{s} + e_{u}) (36 I_{5}[\psi^{a}] + 53 \psi^{a}[u_{0}]) \Big) I[0, 3] \Big]$$

$$+ \frac{e_{u} m_{s} m_{c} \langle \bar{q}q \rangle}{2^{23} \times 5\pi^{5}} I_{3}[\mathcal{S}] I[0, 4]$$

$$- \frac{f_{3\gamma} m_{c}}{2^{24} \times 3 \times 5\pi^{5}} \Big[((2 e_{s} + e_{u}) I_{1}[\mathcal{V}] + 1_{2} (2 e_{d} + e_{u}) I_{3}[\mathcal{V}]) I[0, 5] \Big], \tag{39}$$

$$F_4^{J_\mu^1}(M^2, s_0) = \frac{\langle g_s^2 G^2 \rangle f_{3\gamma} m_c}{2^{27} \times 3^3 \times 5\pi^5} \Big[(11(17e_d + 12e_u)I_3[\mathcal{V}] + 7(2e_s + e_u)\psi^a[u_0])I[0, 2] \Big], \tag{40}$$

where the functions I[n, m], $I_1[\mathcal{F}]$, $I_3[\mathcal{F}]$, and $I_5[\mathcal{F}]$ are listed as

$$I[n,m] = \int_{\mathcal{M}}^{s_0} ds \ e^{-s/M^2} \ s^n (s-\mathcal{M})^m,$$

$$I_1[\mathcal{F}] = \int D_{\alpha_i} \int_0^1 dv \ \mathcal{F}(\alpha_{\bar{q}}, \alpha_q, \alpha_g) \delta'(\alpha_q + \bar{v}\alpha_g - u_0),$$

$$I_3[\mathcal{F}] = \int D_{\alpha_i} \int_0^1 dv \ \mathcal{F}(\alpha_{\bar{q}}, \alpha_q, \alpha_g) \delta(\alpha_q + \bar{v}\alpha_g - u_0),$$

$$I_5[\mathcal{F}] = \int_0^1 du \ \mathcal{F}(u) \delta'(u - u_0),$$

$$(41)$$

where $\mathcal{M} = (2m_c + m_s)^2$, and \mathcal{F} denotes the photon DAs.

The Borel transformation relations employed in the present analysis can be expressed as

$$\mathcal{B}\left\{\frac{1}{\left[[p^2 - m_i^2][(p+q)^2 - m_f^2]\right]}\right\} \to e^{-m_i^2/M_1^2 - m_f^2/M_2^2},\tag{42}$$

on the hadronic representation, and

$$\mathcal{B}\left\{\frac{1}{\left(m^2 - \bar{u}p^2 - u(p+q)^2\right)^{\alpha}}\right\} \to (M^2)^{2-\alpha} \,\delta(u - u_0) \,e^{-m^2/M^2},\tag{43}$$

on the QCD side of the correlation function. The auxiliary parameters entering these transformations are defined as

$$M^2 = \frac{M_1^2 M_2^2}{M_1^2 + M_2^2}, \qquad u_0 = \frac{M_1^2}{M_1^2 + M_2^2}.$$

Here, M_1^2 and M_2^2 denote the Borel mass parameters associated with the initial and final $P_{\psi s}^{\Lambda}$ states, respectively. These parameters arise as a consequence of applying independent Borel transformations to the initial and final hadronic momenta, p^2 and $(p+q)^2$, in order to exponentially suppress contributions from higher-mass states and the continuum part of the spectral density. Since the same physical state $P_{\psi s}^{\Lambda}$ contributes at both the initial and final vertices of the correlation function, the most natural and physically consistent choice is to set $M_1^2 = M_2^2 = 2M^2$, which immediately yields $u_0 = \frac{1}{2}$. This symmetric choice ensures that the single Borel parameter M^2 effectively represents the average virtuality of the heavy-light system and optimally stabilizes the QCD sum rule against numerical uncertainties. Moreover, this parametrization guarantees that the single dispersion integral used in the sum-rule formalism remains convergent and that the ground-state contribution dominates over those from excited resonances and the continuum threshold. In other words, the adopted equality of the Borel parameters provides a balanced exponential suppression on both sides of the correlator, improving the reliability and stability of the extracted form factors and multipole moments. A comprehensive account of this procedure and its applications to heavy exotic systems can be found in Ref. [69].

- [1] S. K. Choi, et al., Observation of a narrow charmonium-like state in exclusive $B^{\pm} \to K^{\pm}\pi^{+}\pi^{-}J/\psi$ decays, Phys. Rev. Lett. 91 (2003) 262001. arXiv:hep-ex/0309032, doi:10.1103/PhysRevLett.91.262001.
- [2] A. Esposito, A. L. Guerrieri, F. Piccinini, A. Pilloni, A. D. Polosa, Four-Quark Hadrons: an Updated Review, Int. J. Mod. Phys. A 30 (2015) 1530002. arXiv:1411.5997, doi:10.1142/S0217751X15300021.
- [3] A. Esposito, A. Pilloni, A. D. Polosa, Multiquark Resonances, Phys. Rept. 668 (2017) 1-97. arXiv:1611.07920, doi: 10.1016/j.physrep.2016.11.002.
- [4] S. L. Olsen, T. Skwarnicki, D. Zieminska, Nonstandard heavy mesons and baryons: Experimental evidence, Rev. Mod. Phys. 90 (1) (2018) 015003. arXiv:1708.04012, doi:10.1103/RevModPhys.90.015003.
- [5] R. F. Lebed, R. E. Mitchell, E. S. Swanson, Heavy-Quark QCD Exotica, Prog. Part. Nucl. Phys. 93 (2017) 143-194. arXiv:1610.04528, doi:10.1016/j.ppnp.2016.11.003.
- [6] M. Nielsen, F. S. Navarra, S. H. Lee, New Charmonium States in QCD Sum Rules: A Concise Review, Phys. Rept. 497 (2010) 41-83. arXiv:0911.1958, doi:10.1016/j.physrep.2010.07.005.
- [7] N. Brambilla, S. Eidelman, C. Hanhart, A. Nefediev, C.-P. Shen, C. E. Thomas, A. Vairo, C.-Z. Yuan, The XYZ states: experimental and theoretical status and perspectives, Phys. Rept. 873 (2020) 1–154. arXiv:1907.07583, doi:10.1016/j.physrep.2020.05.001.
- [8] S. Agaev, K. Azizi, H. Sundu, Four-quark exotic mesons, Turk. J. Phys. 44 (2) (2020) 95-173. arXiv:2004.12079, doi:10.3906/fiz-2003-15.
- [9] H.-X. Chen, W. Chen, X. Liu, S.-L. Zhu, The hidden-charm pentaquark and tetraquark states, Phys. Rept. 639 (2016) 1-121. arXiv:1601.02092, doi:10.1016/j.physrep.2016.05.004.
- [10] A. Ali, J. S. Lange, S. Stone, Exotics: Heavy Pentaquarks and Tetraquarks, Prog. Part. Nucl. Phys. 97 (2017) 123-198. arXiv:1706.00610, doi:10.1016/j.ppnp.2017.08.003.
- [11] F.-K. Guo, C. Hanhart, U.-G. Meißner, Q. Wang, Q. Zhao, B.-S. Zou, Hadronic molecules, Rev. Mod. Phys. 90 (1) (2018) 015004, [Erratum: Rev.Mod.Phys. 94, 029901 (2022)]. arXiv:1705.00141, doi:10.1103/RevModPhys.90.015004.
- [12] Y.-R. Liu, H.-X. Chen, W. Chen, X. Liu, S.-L. Zhu, Pentaquark and Tetraquark states, Prog. Part. Nucl. Phys. 107 (2019) 237–320. arXiv:1903.11976, doi:10.1016/j.ppnp.2019.04.003.
- [13] G. Yang, J. Ping, J. Segovia, Tetra- and penta-quark structures in the constituent quark model, Symmetry 12 (11) (2020) 1869. arXiv:2009.00238, doi:10.3390/sym12111869.
- [14] X.-K. Dong, F.-K. Guo, B.-S. Zou, A survey of heavy-antiheavy hadronic molecules, Progr. Phys. 41 (2021) 65-93. arXiv: 2101.01021, doi:10.13725/j.cnki.pip.2021.02.001.
- [15] X.-K. Dong, F.-K. Guo, B.-S. Zou, A survey of heavy-heavy hadronic molecules, Commun. Theor. Phys. 73 (12) (2021) 125201. arXiv:2108.02673, doi:10.1088/1572-9494/ac27a2.
- [16] H.-X. Chen, W. Chen, X. Liu, Y.-R. Liu, S.-L. Zhu, An updated review of the new hadron states, Rept. Prog. Phys. 86 (2) (2023) 026201. arXiv: 2204.02649, doi:10.1088/1361-6633/aca3b6.
- [17] L. Meng, B. Wang, G.-J. Wang, S.-L. Zhu, Chiral perturbation theory for heavy hadrons and chiral effective field theory for heavy hadronic molecules, Phys. Rept. 1019 (2023) 1–149. arXiv:2204.08716, doi:10.1016/j.physrep.2023.04.003.
- [18] R. Aaij, et al., Observation of $J/\psi p$ Resonances Consistent with Pentaquark States in $\Lambda_b^0 \to J/\psi K^- p$ Decays, Phys. Rev. Lett. 115 (2015) 072001. arXiv:1507.03414, doi:10.1103/PhysRevLett.115.072001.
- [19] R. Aaij, et al., Observation of a narrow pentaquark state, $P_c(4312)^+$, and of two-peak structure of the $P_c(4450)^+$, Phys. Rev. Lett. 122 (22) (2019) 222001. arXiv:1904.03947, doi:10.1103/PhysRevLett.122.222001.
- [20] R. Aaij, et al., Evidence of a $J/\psi\Lambda$ structure and observation of excited Ξ^- states in the $\Xi_b^- \to J/\psi\Lambda K^-$ decay, Sci. Bull. 66 (2021) 1278–1287. arXiv:2012.10380, doi:10.1016/j.scib.2021.02.030.
- [21] R. Aaij, et al., Observation of a J/ $\psi\Lambda$ Resonance Consistent with a Strange Pentaquark Candidate in B- \to J/ $\psi\Lambda$ p⁻ Decays, Phys. Rev. Lett. 131 (3) (2023) 031901. arXiv:2210.10346, doi:10.1103/PhysRevLett.131.031901.
- [22] I. Adachi, et al., Search for Pcs(4459) and Pcs(4338) in Upsilon(1S,2S) inclusive decays at Belle (2 2025). arXiv:2502.
- [23] S. Clymton, H.-C. Kim, T. Mart, Production mechanism of hidden-charm pentaquark states Pcc s with strangeness S=-1, Phys. Rev. D 112 (1) (2025) 014041. arXiv:2504.07693, doi:10.1103/2wvg-jlxp.
- [24] V. L. Chernyak, I. R. Zhitnitsky, B meson exclusive decays into baryons, Nucl. Phys. B 345 (1990) 137–172. doi: 10.1016/0550-3213(90)90612-H.
- [25] V. M. Braun, I. E. Filyanov, QCD Sum Rules in Exclusive Kinematics and Pion Wave Function, Z. Phys. C 44 (1989) 157. doi:10.1007/BF01548594.
- [26] I. I. Balitsky, V. M. Braun, A. V. Kolesnichenko, Radiative Decay Sigma+ —> p gamma in Quantum Chromodynamics, Nucl. Phys. B 312 (1989) 509–550. doi:10.1016/0550-3213(89)90570-1.
- [27] G.-J. Wang, R. Chen, L. Ma, X. Liu, S.-L. Zhu, Magnetic moments of the hidden-charm pentaquark states, Phys. Rev. D 94 (9) (2016) 094018. arXiv:1605.01337, doi:10.1103/PhysRevD.94.094018.
- [28] U. Özdem, K. Azizi, Electromagnetic multipole moments of the $P_c^+(4380)$ pentaquark in light-cone QCD, Eur. Phys. J. C 78 (5) (2018) 379. arXiv:1803.06831, doi:10.1140/epjc/s10052-018-5873-2.
- [29] E. Ortiz-Pacheco, R. Bijker, C. Fernández-Ramírez, Hidden charm pentaquarks: mass spectrum, magnetic moments, and photocouplings, J. Phys. G 46 (6) (2019) 065104. arXiv:1808.10512, doi:10.1088/1361-6471/ab096d.
- [30] Y.-J. Xu, Y.-L. Liu, M.-Q. Huang, The magnetic moment of $P_c(4312)$ as a $\bar{D}\Sigma_c$ molecular state, Eur. Phys. J. C 81 (5) (2021) 421. arXiv:2008.07937, doi:10.1140/epjc/s10052-021-09211-8.

- [31] U. Özdem, Electromagnetic properties of the P_c (4312) pentaquark state, Chin. Phys. C 45 (2) (2021) 023119. doi: 10.1088/1674-1137/abd01c.
- [32] U. Özdem, Magnetic dipole moments of the hidden-charm pentaquark states: $P_c(4440)$, $P_c(4457)$ and $P_{cs}(4459)$, Eur. Phys. J. C 81 (4) (2021) 277. arXiv:2102.01996, doi:10.1140/epjc/s10052-021-09070-3.
- [33] M.-W. Li, Z.-W. Liu, Z.-F. Sun, R. Chen, Magnetic moments and transition magnetic moments of Pc and Pcs states, Phys. Rev. D 104 (5) (2021) 054016. arXiv:2106.15053, doi:10.1103/PhysRevD.104.054016.
- [34] U. Özdem, Electromagnetic properties of D⁻(*)Ξc', D⁻(*)Λc, D⁻s(*)Λc and D⁻s(*)Ξc pentaquarks, Phys. Lett. B 846 (2023) 138267. arXiv:2303.10649, doi:10.1016/j.physletb.2023.138267.
- [35] F.-L. Wang, X. Liu, Higher molecular $P\psi s\Lambda/\Sigma$ pentaquarks arising from the $\Xi c(',*)D^-1/\Xi c(',*)D^-2*$ interactions, Phys. Rev. D 108 (5) (2023) 054028. arXiv:2307.08276, doi:10.1103/PhysRevD.108.054028.
- [36] U. Özdem, Investigation of magnetic moment of Pcs(4338) and Pcs(4459) pentaquark states, Phys. Lett. B 836 (2023) 137635. arXiv:2208.07684, doi:10.1016/j.physletb.2022.137635.
- [37] F. Gao, H.-S. Li, Magnetic moments of hidden-charm strange pentaquark states*, Chin. Phys. C 46 (12) (2022) 123111. arXiv:2112.01823, doi:10.1088/1674-1137/ac8651.
- [38] U. Özdem, Shedding light on the nature of the Pcs(4459) pentaquark state, Phys. Rev. D 111 (7) (2025) 074038. arXiv: 2411.11442, doi:10.1103/PhysRevD.111.074038.
- [39] F. Guo, H.-S. Li, Analysis of the hidden-charm pentaquark states based on magnetic moment and transition magnetic moment, Eur. Phys. J. C 84 (4) (2024) 392. arXiv:2304.10981, doi:10.1140/epjc/s10052-024-12699-5.
- [40] U. Özdem, Magnetic moments of pentaquark states in light-cone sum rules, Eur. Phys. J. A 58 (3) (2022) 46. doi: 10.1140/epja/s10050-022-00700-2.
- [41] F.-L. Wang, S.-Q. Luo, H.-Y. Zhou, Z.-W. Liu, X. Liu, Exploring the electromagnetic properties of the Ξc(',*)D¯s* and Ωc(*)D¯s* molecular states, Phys. Rev. D 108 (3) (2023) 034006. arXiv:2210.02809, doi:10.1103/PhysRevD.108.034006.
- [42] F.-L. Wang, H.-Y. Zhou, Z.-W. Liu, X. Liu, What can we learn from the electromagnetic properties of hidden-charm molecular pentaquarks with single strangeness?, Phys. Rev. D 106 (5) (2022) 054020. arXiv:2208.10756, doi:10.1103/PhysRevD.106.054020.
- [43] U. Özdem, Analysis of the isospin eigenstate $\bar{D}\Sigma_c$, $\bar{D}^*\Sigma_c$, and $\bar{D}\Sigma_c^*$ pentaquarks by their electromagnetic properties, Eur. Phys. J. C 84 (8) (2024) 769. arXiv:2401.12678, doi:10.1140/epjc/s10052-024-13124-7.
- [44] H.-S. Li, F. Guo, Y.-D. Lei, F. Gao, Magnetic moments and axial charges of the octet hidden-charm molecular pentaquark family, Phys. Rev. D 109 (9) (2024) 094027. arXiv:2401.14767, doi:10.1103/PhysRevD.109.094027.
- [45] H.-S. Li, Molecular pentaquark magnetic moments in heavy pentaquark chiral perturbation theory, Phys. Rev. D 109 (11) (2024) 114039. arXiv:2401.14759, doi:10.1103/PhysRevD.109.114039.
- [46] U. Özdem, Investigation on the electromagnetic properties of the $D^{(*)}\Sigma_c^{(*)}$ molecules, Eur. Phys. J. A 61 (1) (2025) 10. arXiv:2405.07273, doi:10.1140/epja/s10050-024-01477-2.
- [47] U. Özdem, Elucidating the nature of hidden-charm pentaquark states with spin-32 through their electromagnetic form factors, Phys. Lett. B 851 (2024) 138551. arXiv:2402.03802, doi:10.1016/j.physletb.2024.138551.
- [48] H. Mutuk, X.-W. Kang, Unveiling the structure of hidden-bottom strange pentaquarks via magnetic moments, Phys. Lett. B 855 (2024) 138772. arXiv:2405.07066, doi:10.1016/j.physletb.2024.138772.
- [49] H. Mutuk, Magnetic moments of hidden-bottom pentaquark states, Eur. Phys. J. C 84 (8) (2024) 874. arXiv:2403.16616, doi:10.1140/epjc/s10052-024-13263-x.
- [50] U. ÖZDEM, Insight into the nature of the $P_c(4457)$ and related pentaquarks, Eur. Phys. J. C 85 (6) (2025) 624. arXiv: 2409.09449, doi:10.1140/epjc/s10052-025-14323-6.
- [51] U. Özdem, Probing the electromagnetic structure of the $P_c(4337)^+$ pentaquark: insights from a diquark-diquark-antiquark picture for $J^P=\frac{1}{2}^-$ and $\frac{3}{2}^-$ states, Eur. Phys. J. C 85 (6) (2025) 704. arXiv:2506.04345, doi:10.1140/epjc/s10052-025-14439-9.
- [52] S.-H. Zhu, F.-L. Wang, X. Liu, Electromagnetic characteristics as probes into the inner structures of the predicted $\Xi_c^{(',*)}D_s^{(*)}$ molecular states (10 2025). arXiv:2510.18492.
- [53] U. Özdem, Unveiling the electromagnetic structure and intrinsic dynamics of spin-3/2 hidden-charm pentaquarks: A comprehensive QCD analysis, Chin. Phys. 49 (10) (2025) 103106. arXiv:2504.13488, doi:10.1088/1674-1137/ade95a.
- [54] Z.-G. Wang, Analysis of the scalar and axial-vector heavy diquark states with QCD sum rules, Eur. Phys. J. C 71 (2011) 1524. arXiv:1008.4449, doi:10.1140/epjc/s10052-010-1524-y.
- [55] R. T. Kleiv, T. G. Steele, A. Zhang, I. Blokland, Heavy-light diquark masses from QCD sum rules and constituent diquark models of tetraquarks, Phys. Rev. D 87 (12) (2013) 125018. arXiv:1304.7816, doi:10.1103/PhysRevD.87.125018.
- [56] H. J. Weber, H. Arenhovel, Isobar Configurations in Nuclei, Phys. Rept. 36 (1978) 277–348. doi:10.1016/0370-1573(78) 90187-4.
- [57] S. Nozawa, D. B. Leinweber, Electromagnetic form-factors of spin 3/2 baryons, Phys. Rev. D 42 (1990) 3567–3571. doi:10.1103/PhysRevD.42.3567.
- [58] V. Pascalutsa, M. Vanderhaeghen, S. N. Yang, Electromagnetic excitation of the Delta(1232)-resonance, Phys. Rept. 437 (2007) 125–232. arXiv:hep-ph/0609004, doi:10.1016/j.physrep.2006.09.006.
- [59] G. Ramalho, M. T. Pena, F. Gross, Electric quadrupole and magnetic octupole moments of the Delta, Phys. Lett. B 678 (2009) 355–358. arXiv:0902.4212, doi:10.1016/j.physletb.2009.06.052.
- [60] Z.-G. Wang, Q. Xin, Analysis of the hidden-charm pentaquark candidates in the $J/\psi\Lambda$ mass spectrum via the QCD sum rules (8 2025). arXiv: 2508.17373.
- [61] I. I. Balitsky, V. M. Braun, Evolution Equations for QCD String Operators, Nucl. Phys. B 311 (1989) 541–584. doi:

- 10.1016/0550-3213(89)90168-5.
- [62] V. M. Belyaev, B. Y. Blok, CHARMED BARYONS IN QUANTUM CHROMODYNAMICS, Z. Phys. C 30 (1986) 151. doi:10.1007/BF01560689.
- [63] P. Ball, V. M. Braun, N. Kivel, Photon distribution amplitudes in QCD, Nucl. Phys. B 649 (2003) 263-296. arXiv: hep-ph/0207307, doi:10.1016/S0550-3213(02)01017-9.
- [64] S. Navas, et al., Review of particle physics, Phys. Rev. D 110 (3) (2024) 030001. doi:10.1103/PhysRevD.110.030001.
- [65] B. L. Ioffe, QCD at low energies, Prog. Part. Nucl. Phys. 56 (2006) 232-277. arXiv:hep-ph/0502148, doi:10.1016/j. ppnp.2005.05.001.
- [66] S. Narison, $\overline{m}_{c,b}$, $<\alpha_s G^2>$ and α_s from Heavy Quarkonia, Nucl. Part. Phys. Proc. 300-302 (2018) 153–164. doi: 10.1016/j.nuclphysbps.2018.12.026.
- [67] J. Rohrwild, Determination of the magnetic susceptibility of the quark condensate using radiative heavy meson decays, JHEP 09 (2007) 073. arXiv:0708.1405, doi:10.1088/1126-6708/2007/09/073.
- [68] U. Özdem, Investigating the underlying structure of vector hidden-charm tetraquark states via their electromagnetic characteristics, Phys. Rev. D 111 (5) (2025) 054009. arXiv:2412.06447, doi:10.1103/PhysRevD.111.054009.
- [69] U. Özdem, Unveiling the underlying structure of axial-vector bottom-charm tetraquarks in the light of their magnetic moments, JHEP 05 (2024) 301. arXiv:2403.16191, doi:10.1007/JHEP05 (2024) 301.
- [70] K. Azizi, U. Özdem, Exploring the magnetic dipole moments of $T_{QQ\overline{qs}}$ and $T_{QQ\overline{qs}}$ states in the framework of QCD light-cone sum rules, JHEP 03 (2023) 166. arXiv:2301.07713, doi:10.1007/JHEP03(2023)166.
- [71] K. U. Can, G. Erkol, B. Isildak, M. Oka, T. T. Takahashi, Electromagnetic properties of doubly charmed baryons in Lattice QCD, Phys. Lett. B 726 (2013) 703-709. arXiv:1306.0731, doi:10.1016/j.physletb.2013.09.024.
- [72] K. U. Can, G. Erkol, B. Isildak, M. Oka, T. T. Takahashi, Electromagnetic structure of charmed baryons in Lattice QCD, JHEP 05 (2014) 125. arXiv:1310.5915, doi:10.1007/JHEP05(2014)125.
- [73] I. Vujmilovic, S. Collins, L. Leskovec, S. Prelovsek, Electromagnetic form factors and structure of the T_{bb} tetraquark from lattice QCD (10 2025). arXiv:2510.17549.